

Article

Chemically Synthesized Iron-Oxide-Based Pure Negative Electrode for Solid-State Asymmetric Supercapacitor Devices

A. A. Yadav ^{1,†}, Y. M. Hunge ^{2,†}, Seongjun Ko ¹ and Seok-Won Kang ^{1,*}
¹ Department of Automotive Engineering, Yeungnam University, 280 Daehak-ro, Gyeongsan 38541, Korea

² Division of Biotechnology, Daegu Gyeongbuk Institute of Science and Technology (DGIST), Daegu 42988, Korea

* Correspondence: swkang@yu.ac.kr

† These authors contributed equally to this work.

Abstract: Among energy storage devices, supercapacitors have received considerable attention in recent years owing to their high-power density and extended cycle life. Researchers are currently making efforts to improve energy density using different asymmetric cell configurations, which may provide a wider potential window. Many studies have been conducted on positive electrodes for asymmetric supercapacitor devices; however, studies on negative electrodes have been limited. In this study, iron oxides with different morphologies were synthesized at various deposition temperatures using a simple chemical bath deposition method. A nanosphere-like morphology was obtained for α -Fe₂O₃. The obtained specific capacitance (C_s) of α -Fe₂O₃ was 2021 F/g at a current density of 4 A/g. The negative electrode showed an excellent capacitance retention of 96% over 5000 CV cycles. The fabricated asymmetric solid-state supercapacitor device based on α -Fe₂O₃-NF//Co₃O₄-NF exhibited a C_s of 155 F/g and an energy density of 21 Wh/kg at 4 A/g.

Keywords: chemical bath deposition; α -Fe₂O₃; Co₃O₄; supercapacitor device



Citation: Yadav, A.A.; Hunge, Y.M.; Ko, S.; Kang, S.-W. Chemically Synthesized Iron-Oxide-Based Pure Negative Electrode for Solid-State Asymmetric Supercapacitor Devices. *Materials* **2022**, *15*, 6133. <https://doi.org/10.3390/ma15176133>

Academic Editors: Edward Song, Gaurab Dutta, Erica Murray and Francisco Carrasco-Marín

Received: 27 May 2022

Accepted: 29 August 2022

Published: 3 September 2022

Publisher's Note: MDPI stays neutral with regard to jurisdictional claims in published maps and institutional affiliations.



Copyright: © 2022 by the authors. Licensee MDPI, Basel, Switzerland. This article is an open access article distributed under the terms and conditions of the Creative Commons Attribution (CC BY) license (<https://creativecommons.org/licenses/by/4.0/>).

1. Introduction

Currently, energy storage and conversion are the major issues in sustainable development, and renewable energy sources are sufficient to fulfill the increasing demand for global energy [1]. In the case of conventional energy storage devices, few limitations exist in the development of energy storage devices with good performance and efficiency [2]. Compared to conventional energy storage devices, supercapacitors are emerging energy storage devices with good cyclic stability, a rapid charge–discharge rate with high-power density, enhanced temperature range, and long cycle life, which may meet the ever-growing demand for energy storage devices [3]. Depending on the charge storage mechanism, supercapacitors are mainly categorized into two types: (1) electric double-layer (EDLC) supercapacitors and (2) pseudocapacitors [4]. EDLCs predominantly exhibit capacitance developed from charge accumulation (non-Faradaic) that occurs at the electrode–electrolyte interface [5]. In pseudocapacitors, pseudocapacitance is mainly caused by the redox reactions that occur in electrolytes and the electrically active surface of the electrode material [6]. In particular, transition metal oxides and polymers have predominantly been studied as pseudocapacitor materials [7]. The transition metal oxides, such as NiO, Co₃O₄, and MnO₂, and double metal oxides, such as MCo₂O₄ (M = Mn, Ni, Fe), are used as positive electrodes [7–11]. However, in the case of an asymmetric solid-state supercapacitor (ASC) device, the performance depends on both positive and negative electrodes. The capacitance of the cell was measured using the following formula [12]:

$$\frac{1}{C} = \frac{1}{C_+} + \frac{1}{C_-} \quad (1)$$

where C_+ and C_- are the specific capacitances (C_s) of the anode and cathode, respectively. According to a study, the C_s values observed in the case of the anode are higher than those of the cathode [13]. Therefore, identifying negative electrode materials with an enhanced electrochemical performance is challenging. Among the transition metal oxides, iron oxide has emerged as a potential negative electrode material. Fe_2O_3 is a naturally abundant metal oxide; it shows a more negative working potential with higher stability in alkaline electrolytes, in addition to a high theoretical capacity (3625 F/g) [9,14]. In the case of Fe_2O_3 , the charges are mainly stored using Faradaic redox reactions that occur between the Fe^{3+} and Fe^{2+} ions and the electrolyte at the interface of the electrode and electrolyte [15–18]. Compared to other metallic oxides, $\alpha\text{-Fe}_2\text{O}_3$ is a good pseudocapacitive material. This may be due to its special crystal structure, such as $\alpha\text{-Fe}_2\text{O}_3$ (hematite), which has a steadier hexagonal-like crystal structure [19]. However, there are a few limitations in the usage of $\alpha\text{-Fe}_2\text{O}_3$ as an electrode material, such as low electrical conductivity, and the particle size of $\alpha\text{-Fe}_2\text{O}_3$ increases with the number of charge–discharge cycles [20].

Therefore, efforts are prevailing to design different nanostructured morphologies of iron oxide directly grown on conducting nickel foam (NF) substrates. The nanostructured porous morphology of $\alpha\text{-Fe}_2\text{O}_3$ is suitable for improving the electrochemical performance because of the presence of a large number of active sites, which provide a large active surface area for charging–discharging reactions [18,19]. These active sites help in reducing the diffusion length and transfer resistance of electrons, which helps sustain a constant rate capability at high resistance [21]. Herein, $\alpha\text{-Fe}_2\text{O}_3$ films were grown directly on NF substrates using a simple chemical bath deposition (CBD) method at different deposition temperatures. At 363 K, porous nonspherical particles of $\alpha\text{-Fe}_2\text{O}_3$ were formed directly on the conducting NF substrate. For the fabrication of the ASC device, $\text{Co}_3\text{O}_4\text{-NF}$ was used as the positive electrode, and the synthesized $\alpha\text{-Fe}_2\text{O}_3\text{-NF}$ electrode was used as the negative electrode. This ASC device showed a good energy density of 21.5 Wh k/g. The negative electrode show a good stability of 96% with improved C_s of 1037 F/g for KOH-based electrolytes.

2. Materials and Methods

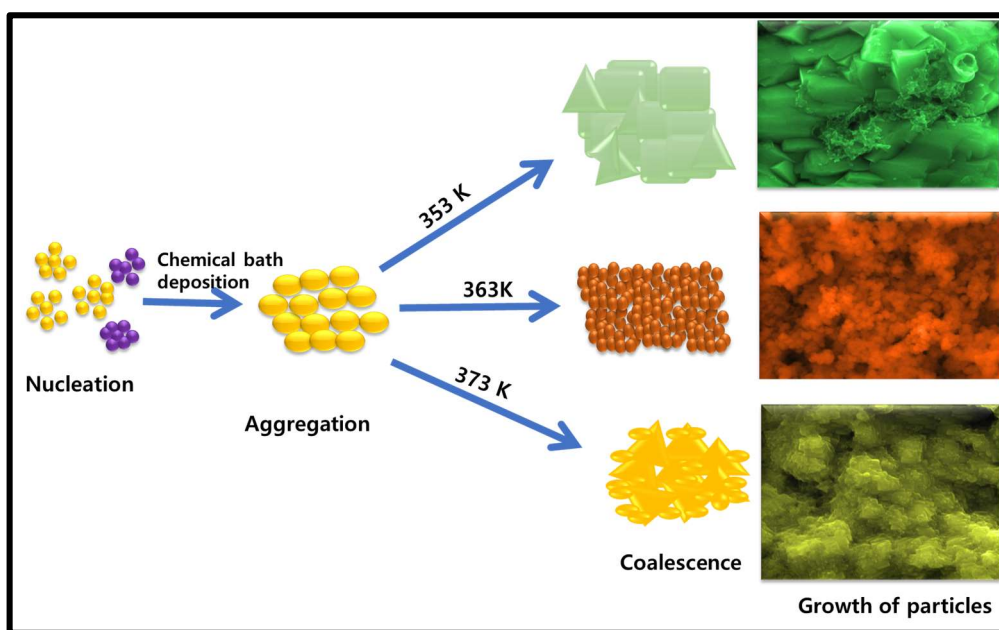
2.1. Synthesis of Negative $\alpha\text{-Fe}_2\text{O}_3\text{-NF}$ Electrode

The $\alpha\text{-Fe}_2\text{O}_3$ thin films were synthesized using a simple CBD method. Briefly, 0.1 M $[\text{Fe}(\text{NO}_3)_3 \cdot 6\text{H}_2\text{O}]$ (ferric nitrate) was dissolved in 25 mL of deionized water (DI) and kept under continuous stirring, and then 0.2 M $[\text{CO}(\text{NH}_2)_2]$ (urea) was dissolved in the mixture and stirred for 25 min to form a uniform reaction mixture. A thoroughly cleaned NF substrate was then inserted into the solvent mixture. The beaker containing the reaction mixture was then kept in a constant-temperature water bath at different deposition temperatures, such as 353 (S1), 363 (S2), and 373 K (S3), for 3 h [22].

After deposition, the brown thin film was removed from the bath, washed repeatedly with DI water, and dried at room temperature for 5 h. A schematic of the synthesis of $\alpha\text{-Fe}_2\text{O}_3$ is shown in Scheme 1. In addition, the brown Fe_2O_3 thin film confirmed the formation of $\alpha\text{-Fe}_2\text{O}_3$ nanoparticles.

2.2. Synthesis of the Positive $\text{Co}_3\text{O}_4\text{-NF}$ Electrode

In the facile synthesis of the positive electrode, $\text{Co}_3\text{O}_4\text{-NF}$ was synthesized using a previously reported CBD method [23]. A reaction mixture of 0.1 M $[\text{Co}(\text{NO}_3)_2]$ (cobalt nitrate) and 0.2 M $[\text{CO}(\text{NH}_2)_2]$ (urea) was formed in 25 mL of DI water. This reaction mixture and the cleaned NF substrate were maintained at 363 K for 5 h. The as-deposited thin films were dried in air and annealed at 623 K.



Scheme 1. Schematic of synthesis of α -Fe₂O₃.

3. Results and Discussion

3.1. Structural and Morphological Characterization of the Negative α -Fe₂O₃-NF Electrode

The XRD patterns of the S1, S2, and S3 thin films are shown in Figure 1a. The observed high-intensity peaks correspond to (012), (104), (110), (113), (024), (116), (214), and (300) planes and match well with the JCPDS card no. 79-0007. The α phase of the Fe₂O₃ thin film formation is confirmed by the peak position [24]. The different deposition temperatures affected the nucleation rate, surface structure, and growth direction of the α -Fe₂O₃ thin films. For the S2 sample, the observed high-intensity peaks correspond to the (013), (104), and (115) planes. Further, the intensities of the XRD peaks for the S1 sample decreased due to the incomplete growth of particles, while in the case of the S3 sample, the film peeled up from the NF substrate; therefore, it showed a low intensity [25]. The crystal structure of α -Fe₂O₃ was reproduced using the VISTA software, as shown in Figure 1b. The brown and red balls represent the Fe and O elements, respectively, and the CIF file was downloaded from the crystallography open database [26]. XPS analysis was performed to study the composition and bonding of α -Fe₂O₃. The survey scan spectra of α -Fe₂O₃ are shown in Figure 1c. The high-resolution survey scan spectra confirmed the presence of Fe 2p, O 1s, and C 1s. The Fe 2p spectrum shows two pronounced peaks positioned at 711.4 (Fe 2p_{3/2}) and 724.4 eV (Fe 2p_{1/2}), respectively (Figure 1d). The binding energy difference between the two peaks is 13.5 eV, which agrees well with the previously reported literature for the Fe 2p spectrum [27]. The two satellite peaks are present near the main peak at the binding energies of 719.2 and 732.4 eV, which shows that the oxidation phase is Fe³⁺. The O 1s core-level peak was resolved into two peaks at binding energies of 529.4 and 531.2 eV (Figure 1e) [28]. The peak at 529.4 eV was mainly due to lattice oxygen (FeO), and that at 531.2 eV was due to surface hydroxyl (–OH) [29,30].

Figure 2 shows the surface morphologies of the α -Fe₂O₃ thin films (S1, S2, and S3). At low temperatures, the rhombohedra with connected edge-like morphologies were obtained for the S1 sample (Figure 2a–c). In addition, owing to the low reaction temperature, the rate of reaction was reduced, which affected the process of thin-film formation, such as nucleation, aggregation, and growth [31,32]. A further increase in deposition temperature resulted in nanosphere-like morphology, as shown in Figure 2d–f. The particle size was found in the range of 30–40 nm from the SEM observation. This nanosphere-like morphology mainly enhances the electrochemical properties. At higher temperatures, agglomeration of the particles occurred (Figure 2g–i). The morphology of α -Fe₂O₃ was

further confirmed using TEM. Figure 3a,b show the TEM images of S2, which are in good agreement with the SEM data.

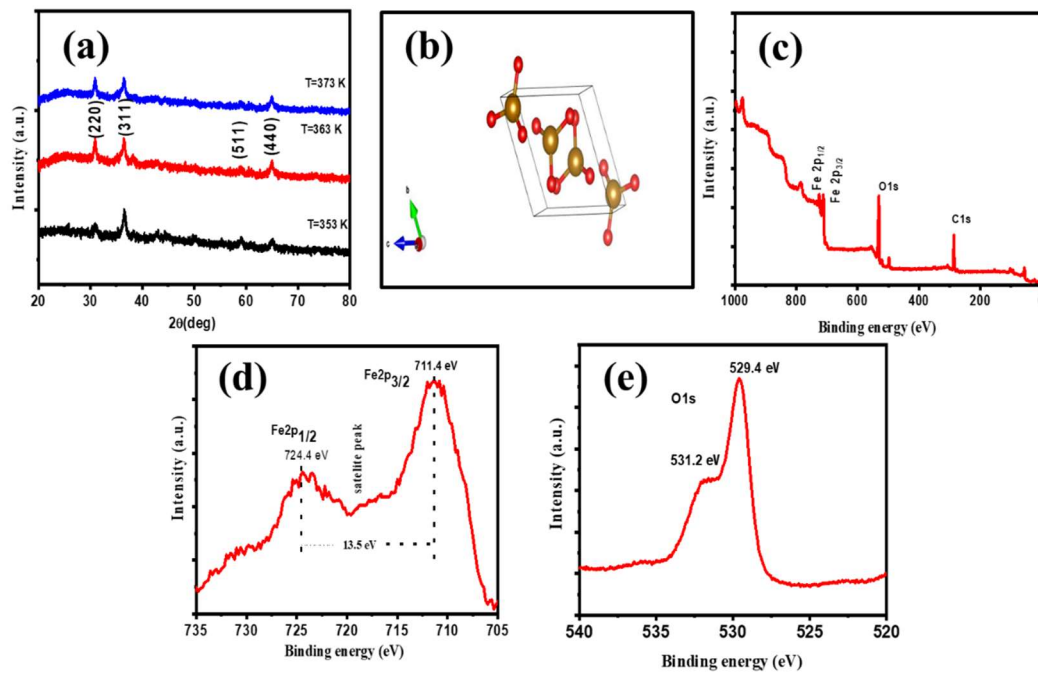


Figure 1. (a) XRD patterns of α -Fe₂O₃ at different deposition temperatures. (b) Crystal structure of α -Fe₂O₃. Brown and red balls represent Fe and O elements. XPS study for α -Fe₂O₃ (c) survey scan spectra, (d) Fe 2p core-level spectrum, and (e) O 1s core-level spectrum.

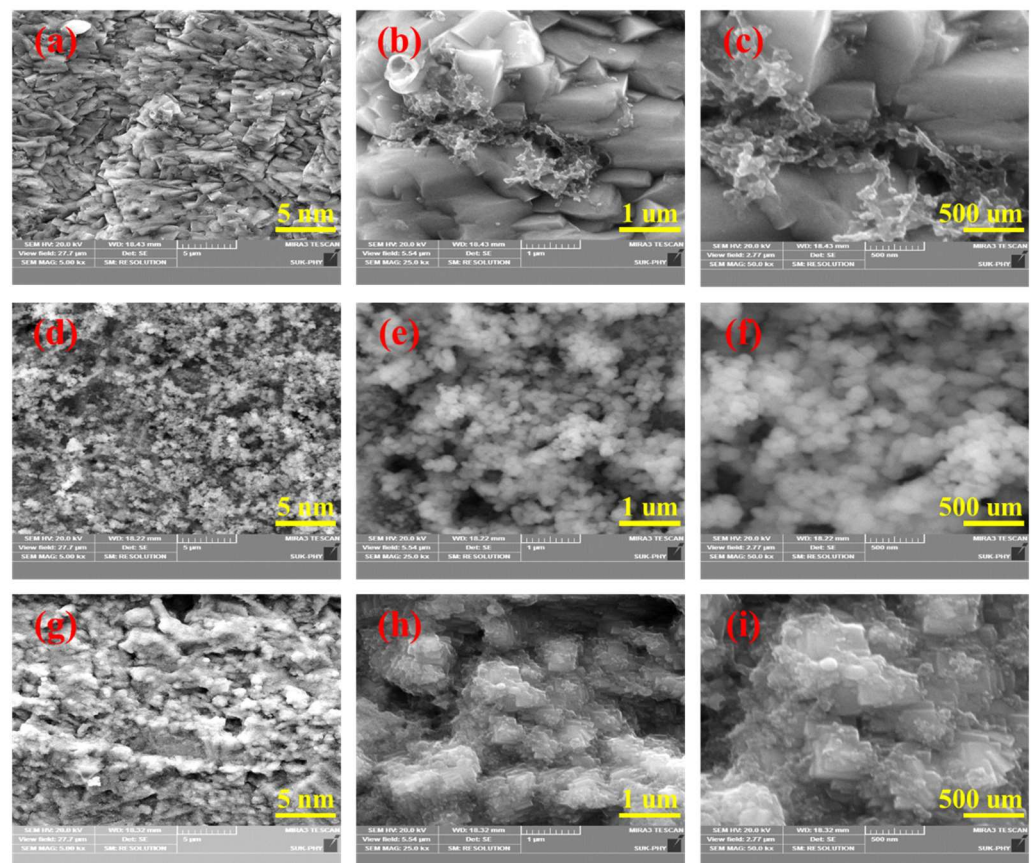


Figure 2. (a–c) SEM images of S1, (d–f) S2, and (g–i) S3 thin films at different magnifications.

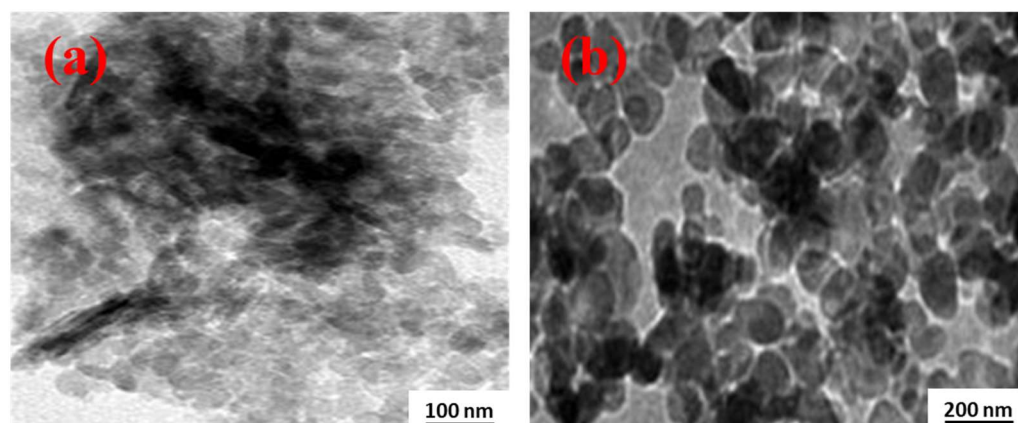
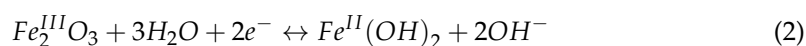


Figure 3. (a,b) TEM images of α -Fe₂O₃.

3.2. Electrochemical Performance of the α -Fe₂O₃-NF Electrode

Figure 4a shows the CV curves of the S1, S2, and S3 samples at 100 mV/s. The area under the curve for the S2 sample was greater than that of the S1 and S3 samples. The electrochemical study for the negative α -Fe₂O₃-NF electrode (S2) was tested in a 2 M KOH electrolyte in the operating potential window range from 0.0 to −1.0 V Ag/AgCl. The CVs of the α -Fe₂O₃-NF electrodes were studied at various scan rates (Figure 4b). The CV curves for α -Fe₂O₃-NF at −1 and −1.2 V are shown in Figure A1. The shape of the CV curve was semi-rectangular, owing to the reversible redox reactions occurring between the Fe³⁺ and Fe²⁺ ions in the KOH electrolyte. This study substantiates the pseudocapacitive nature of the α -Fe₂O₃ electrode [32]. At lower scan rates, such as 5 mV/s, the available duration for the OH[−] ions in the electrolyte (KOH) to intercalate with the electrode material (α -Fe₂O₃-NF) is the maximum, which may be responsible for the enhancement of C_s. The charging mechanism in the α -Fe₂O₃-NF electrode is shown in the following reaction [33,34]:



The GCD curves for α -Fe₂O₃ at various current densities in the operating window, ranged from 0.0 to −1.0 V Ag/AgCl, are shown in Figure 4c. The GCD curve shows the nonlinear nature of the discharge curve owing to the redox reactions occurring at the interface. The C_s value of the α -Fe₂O₃ electrode at a current density of 4 A/g was 2125 F/g, which was calculated using Equation (A1) in the Appendix. The cyclic stability performance also decreased after 5000 GCD cycles, as shown in Figure A2. Figure 4d shows the variations in C_s with various current densities. The inset of Figure 4e shows the stability of the α -Fe₂O₃-NF electrode, tested using CV cycling at 100 mV/s (scan rate) for 5000 CV cycles. Figure 4e shows the plot of capacity retention vs. cycle number, and the observed electrochemical stability of the α -Fe₂O₃-NF electrode was 96%. The improved performance of the α -Fe₂O₃-NF electrode was predominantly due to its porous morphology, which decreases the diffusion length and increases the rate capability. In addition, the α -Fe₂O₃ nanospheres were strongly attached to the conductive NF substrate, which prevented the loss of the active material during the cyclic stability performance study. The electrochemical performance of the α -Fe₂O₃-NF electrode is given in Table A1 (Appendix A). Therefore, the nanosphere-like α -Fe₂O₃-NF electrode is suitable for use as a negative electrode in the fabrication of ASC devices. The calculated b-value is 0.7 at the cathodic potential, which is close to 0.5, rather than 1, proving that the charge storage mechanism originates from the dominant diffusion-controlled process, as shown in Figure A3a. In addition, Figure A3b shows the capacitive and diffusive current-controlled distribution for the α -Fe₂O₃ electrode [35].

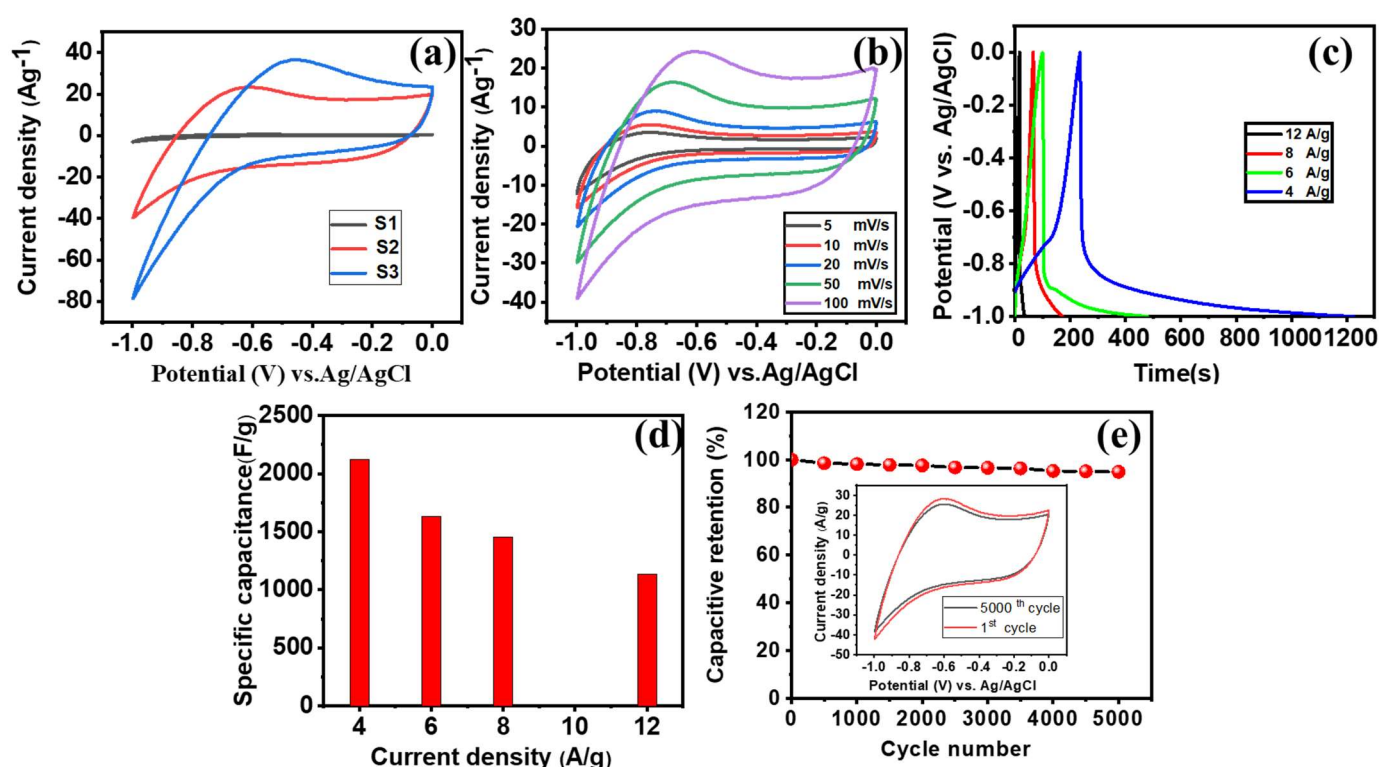


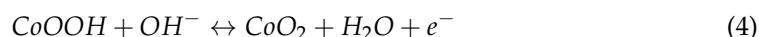
Figure 4. CV study for (a) S1, S2, and S3 samples, and (b) different scan rates; (c) GCD curves at different current densities; (d) plot of specific capacitance vs. current density; (e) plot of capacity retention vs. cycle number and inset shows the stability study at 5000 CV cycles for the $\alpha\text{-Fe}_2\text{O}_3$ thin film.

3.3. Structural and Morphological Characterization of the Positive Co_3O_4 -NF Electrode

A nanowire-like Co_3O_4 -NF thin film was synthesized using a facile CBD method. The XRD pattern of the deposited Co_3O_4 is shown in Figure 5a. The peaks observed at 31.4° , 36.9° , 44.9° , 59.4° , and 65.3° are indexed to planes corresponding to (220), (311), (400), (422), and (511), respectively, according to JCPDS card no:42-1467. Figure 5b shows the FE-SEM image for Co_3O_4 -NF. The observed nanowire-like morphology is uniformly distributed on the surface of the NF substrate. The nanowire-like morphology of Co_3O_4 -NF provides less resistance value and porous structure, which improves the reaction rate [36]. Figure 5c,d show the TEM images of the Co_3O_4 -NF electrode, which substantiates its nanowire-like nature.

3.4. Electrochemical Performance of the Positive Co_3O_4 -NF Electrode

The electrochemical study of the Co_3O_4 -NF electrode was conducted in a 2 M KOH electrolyte. The CV curves of the Co_3O_4 -NF electrode are shown in Figure 6a. The CV curves for the Co_3O_4 -NF electrode show the presence of a pair of redox peaks, which originate from the Faradaic reactions that occur at the electrode surface, and are presented below [37–39]:



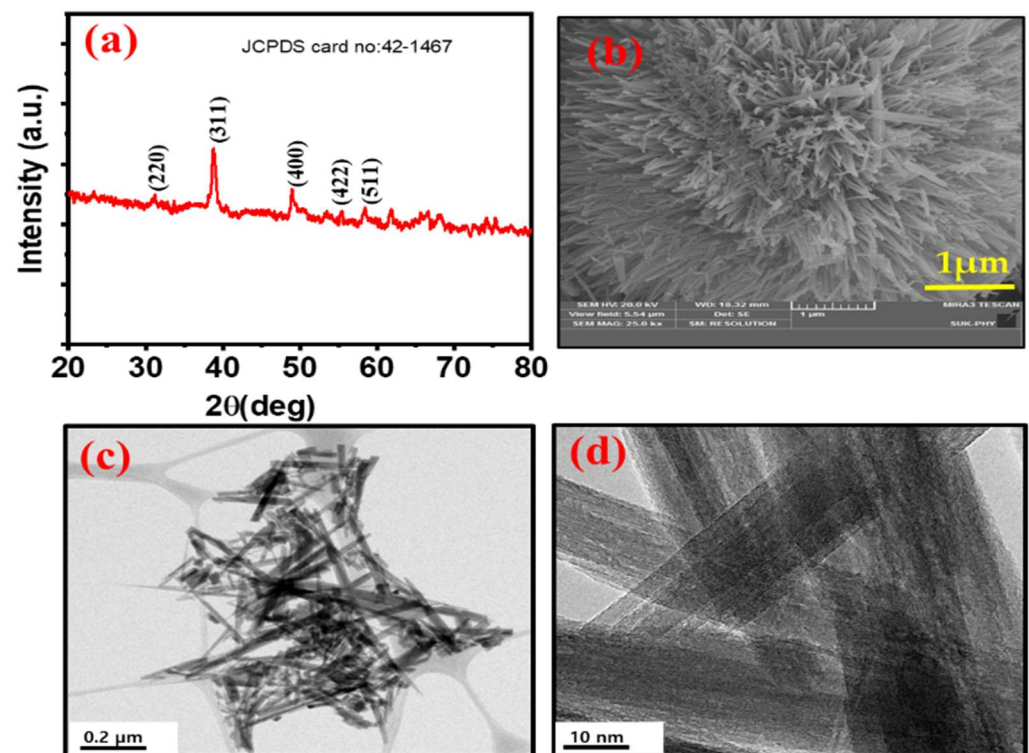


Figure 5. (a) XRD pattern, (b) SEM images, and (c,d) TEM images for the Co₃O₄ thin film.

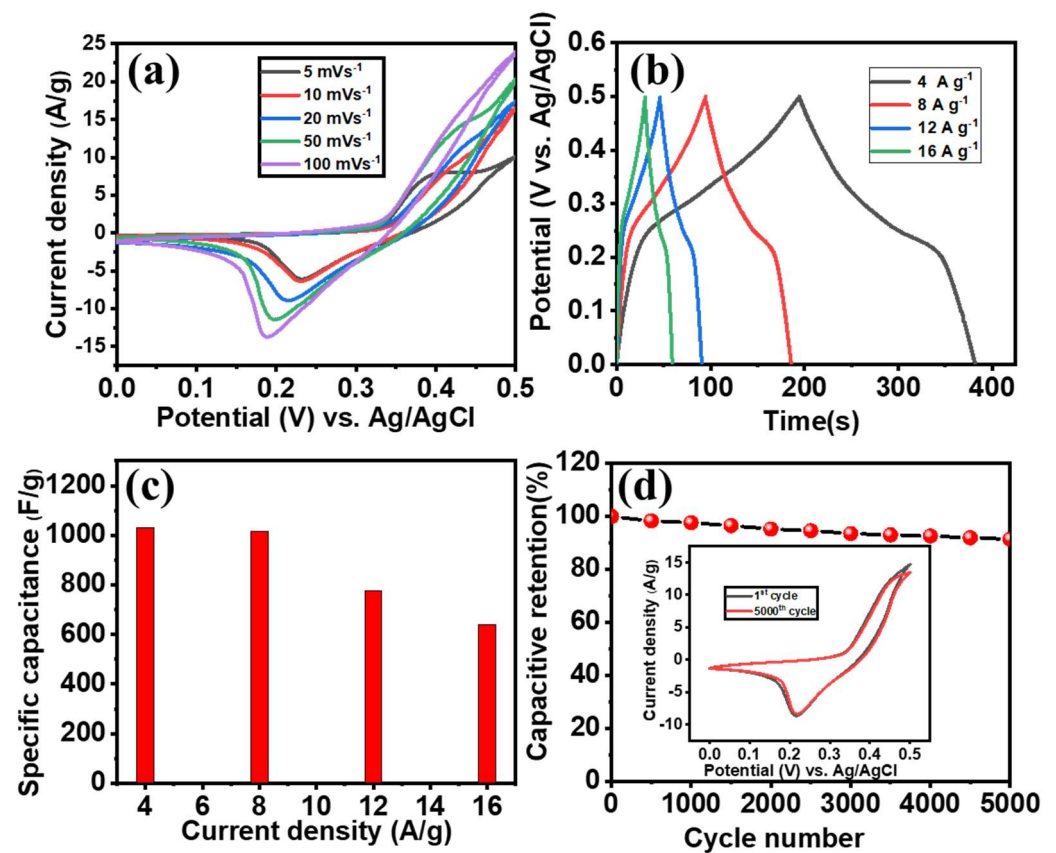


Figure 6. (a) CV curves at different scan rates, (b) GCD curves at different current densities, (c) plot of specific capacitance vs. current density, (d) plot of capacity retention vs. cycle number, and the inset shows the stability study at 5000 CV cycles for the Co₃O₄-NF thin film.

The GCD curve of the Co_3O_4 -NF electrode is shown in Figure 6b. The GCD curve exhibits a nearly symmetric nature with the same charging and discharging times and a low value of internal resistance [39]. Figure 6c displays C_s observed at various current densities. The C_s value observed at 4 A/g is approximately 1032 F/g. The cyclic stability of the Co_3O_4 -NF electrode studied for the 5000th CV cycle is presented in Figure 6d, and the inset shows the stability study at 5000 CV cycles for the Co_3O_4 -NF thin film. The observed b-value is 0.45 at the cathodic potential, which is close to 0.5, rather than 1, as shown in Figure A3c. This indicates that the charge storage contributions originate from the dominant diffusion-controlled processes. Figure A3d shows the capacitive and diffusion-controlled contributions of the Co_3O_4 -NF electrode. As the scan rate increased, the capacitive contribution to the total charge increased. A major diffusion-controlled process for the Co_3O_4 -NF electrode was observed at all of the scan rates, which is consistent with the battery-type nature of the electrode during the charge/discharge process.

3.5. Supercapacitive Performance of the Solid-State Co_3O_4 -NF// α - Fe_2O_3 -NFASC Device

In this study, an ASC device was fabricated using Co_3O_4 -NF and α - Fe_2O_3 -NF as the positive and negative electrodes, respectively, with PVA-KOH as the solid-state electrolyte (Figure 7a). The charges across the Co_3O_4 -NF and α - Fe_2O_3 -NF electrodes were balanced using Equation (1). The mass loaded on both positive (Co_3O_4 -NF) and negative electrodes (α - Fe_2O_3 -NF) are 1.85 and 2.15 mg/cm², respectively. Figure 7b shows the CV profile of the Co_3O_4 -NF// α - Fe_2O_3 -NF ASC device at various scan rates in the potential window of 0–1.0 V. The specific capacitance calculated for the Co_3O_4 -NF// α - Fe_2O_3 -NF device was approximately 164 F/g, as shown in Figure 7c. In the case of electrochemical double-layer capacitance, the ideal shape of the CV is rectangular, and the mirror image and current density are independent of the operating potential of the energy storage device during the discharge process [40]. The CV curves for the ASC device at different angles, such as 0°, 45°, 90°, 120°, and 180°, are shown in Figure A4a (Appendix A). The shape of the CV curve is not an ideal rectangular redox peak, and the shapes of the CV curves do not change [41–43]. The GCD curves for the Co_3O_4 -NF// α - Fe_2O_3 -NF ASC device at current densities of 4–12 A/g are shown in Figure 8a. The GCD curves show nearly symmetric charge–discharge curves. In addition, the voltage plateaus observed in all of the GCD curves confirm the contribution of the capacitance originating from the pseudocapacitive nature of the electrode [42]. The C_s values calculated from the GCD curves were plotted as a function of the current density (Figure 8b). The device delivered a high C_s of 160 F/g at 4 A/g. Figure A4b shows the Ragone plot of the energy density vs. power density for the fabricated Co_3O_4 -NF// α - Fe_2O_3 -NF ASC device. The maximum energy density of the device was observed up to 21.5 Wh/kg at a power density of 158.2 W/kg and a current density of 4 g^{−1}. Table A2 in Appendix A shows the electrochemical performance of the ASC device, based on Co_3O_4 -NF// α - Fe_2O_3 -NF. The stability of the Co_3O_4 -NF// α - Fe_2O_3 -NF ASC device was tested using the GCD technique for 10,000 cycles. The capacitance retention of the Co_3O_4 -NF// α - Fe_2O_3 -NF ASC device is approximately 92%, as shown in Figure 8c. In addition, no significant difference was observed in the GCD curves before and after the stability study (Figure 8c). Furthermore, the electrochemical properties of the Co_3O_4 -NF// α - Fe_2O_3 -NF ASC device were studied using EIS. Figure 8d shows the Nyquist plot for the Co_3O_4 -NF// α - Fe_2O_3 -NF ASC device in the frequency range of 5 kHz to 50 MHz (5 mV), and the inset shows the high-frequency region. The obtained values of series resistance (R_s) and charge transfer resistance (R_{ct}) for the Co_3O_4 -NF// α - Fe_2O_3 -NF ASC device are 0.15 and 2.5 Ω /cm², respectively. Thus, the ACS device based on Co_3O_4 -NF// α - Fe_2O_3 -NF exhibited good electrochemical properties.

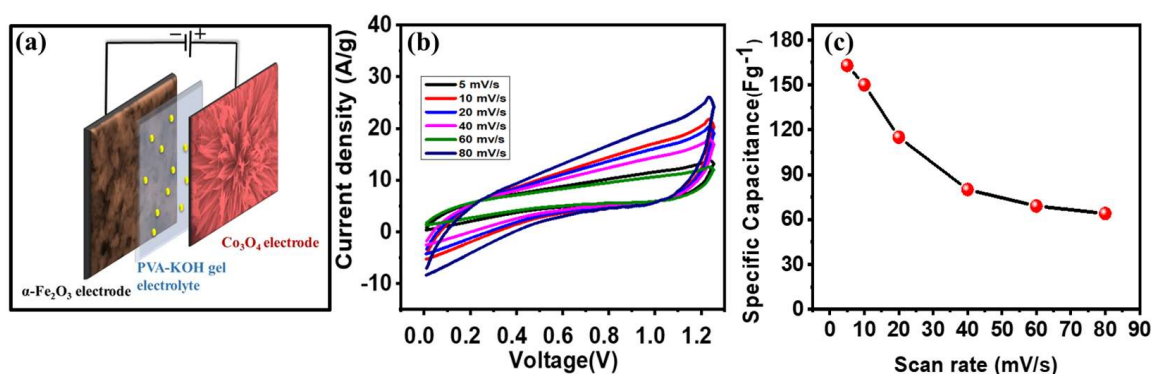


Figure 7. (a) Schematic of the supercapacitor device, (b) CV curves at different scan rates for the $\text{Co}_3\text{O}_4\text{-NF} // \alpha\text{-Fe}_2\text{O}_3\text{-NF}$ ASC device, (c) variation in specific capacitance at different scan rates for the $\text{Co}_3\text{O}_4\text{-NF} // \alpha\text{-Fe}_2\text{O}_3\text{-NF}$ ASC device.

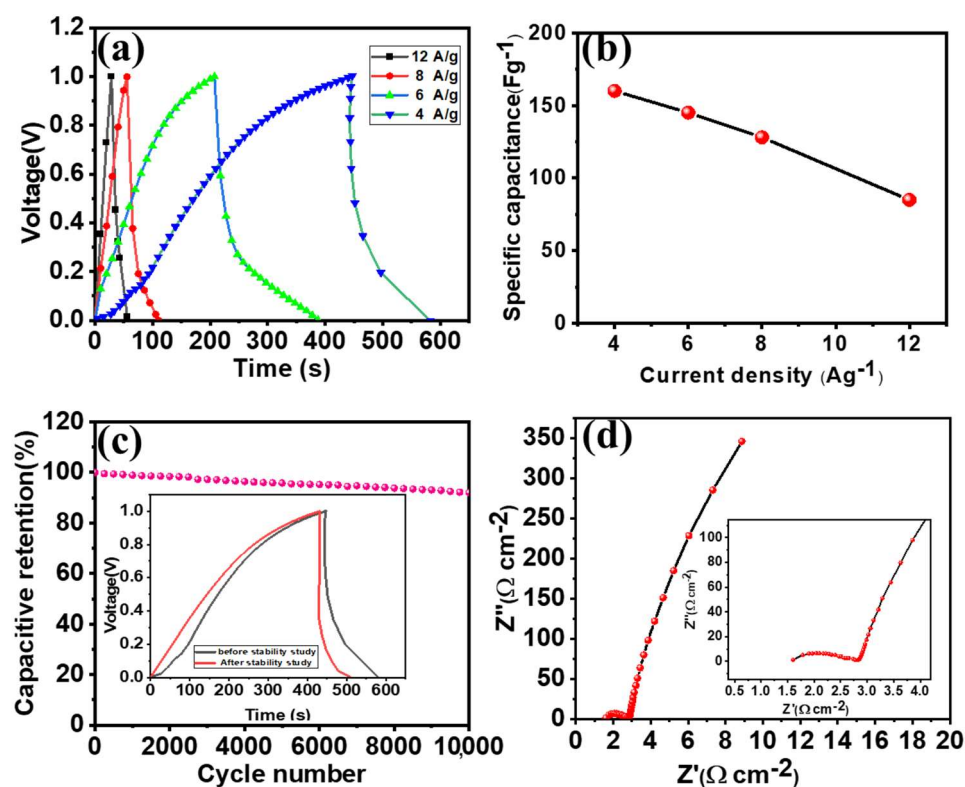


Figure 8. (a) GCD curves, (b) variation in specific capacitance at different current densities, (c) capacitive retention study, and inset show stability study, (d) Nyquist plot, and the inset shows the high-frequency region for the $\text{Co}_3\text{O}_4\text{-NF} // \alpha\text{-Fe}_2\text{O}_3\text{-NF}$ ASC device.

4. Conclusions

Nanosphere-like $\alpha\text{-Fe}_2\text{O}_3$ was uniformly deposited on an NF substrate using a simple CBD technique. The porous nature of $\alpha\text{-Fe}_2\text{O}_3$ contributed to its good specific capacitance with enhanced cyclic stability. The $\text{Co}_3\text{O}_4\text{-NF} // \alpha\text{-Fe}_2\text{O}_3\text{-NF}$ device, fabricated using $\text{Co}_3\text{O}_4\text{-NF}$ and $\alpha\text{-Fe}_2\text{O}_3\text{-NF}$ as the positive and negative electrodes, respectively, shows the maximum specific capacitance (C_s) of 164 F/g at a current density of 4 A/g. The maximum energy density of the device was observed up to 21.5 Wh/kg at a power density of 158.2 W/kg, with excellent rate capability. In addition, the $\text{Co}_3\text{O}_4\text{-NF} // \alpha\text{-Fe}_2\text{O}_3\text{-NF}$ ASC device showed a capacitance retention of 92% after 10,000 cycles of GCD. The outstanding performance of $\alpha\text{-Fe}_2\text{O}_3\text{-NF}$ makes it one of the favorable negative electrode materials for high-performance energy storage devices.

Author Contributions: Conceptualization, S.-W.K.; methodology, A.A.Y.; formal analysis, A.A.Y.; investigation, A.A.Y. and S.K.; resources, S.-W.K.; writing—original draft preparation, A.A.Y.; writing—review and editing, A.A.Y., Y.M.H. and S.-W.K.; supervision, S.-W.K.; validation, S.K.; visualization, S.K.; project administration, S.-W.K.; funding acquisition, S.-W.K. All authors have read and agreed to the published version of the manuscript.

Funding: This work was supported by the National Research Foundation of Korea (NRF) grant funded by the Korean government (MSIT) (No. 2019R1A5A8080290). In addition, this work was partly supported by the Korea Institute of Energy Technology Evaluation and Planning (KETEP) grant funded by the Korean government (MOTIE) (20214000000010, Gyeongbuk Regional Wind Energy Cluster Human Resources Development Project).

Institutional Review Board Statement: Not applicable.

Informed Consent Statement: Not applicable.

Data Availability Statement: The data presented in this study are available on request from the corresponding author. The data are not publicly available.

Conflicts of Interest: The authors declare no conflict of interest.

Appendix A

Appendix A.1. Materials Characterization

The formation of α -Fe₂O₃-NF and Co₃O₄-NF was confirmed by X-ray diffraction (XRD, Bruker AXS D8 advance model) analysis. The surface morphology of α -Fe₂O₃-NF and Co₃O₄-NF was examined by field emission scanning electron microscopy (FE-SEM) and transmission electron microscopy (TEM). X-ray photoelectron spectroscopy (XPS) analysis of the powdered sample (~1–5 mg) of α -Fe₂O₃-NF was performed to determine the chemical composition and oxidation states (X-ray source: monochromatic Al K α , ultimate energy resolution and I_t = 0.50 eV FWHM, Ag3d intensity curve).

Appendix A.2. Electrochemical Characterization

The electrochemical performances of the α -Fe₂O₃-NF and Co₃O₄-NF electrodes were tested using a three-electrode system on a ZIVE SP2 battery cycler. In the case of the three-electrode system, α -Fe₂O₃-NF and Co₃O₄-NF electrodes (1 cm²) were used as the working electrodes, platinum wire as the counter electrode, and Ag/AgCl as the reference electrode. The electrochemical properties were tested in a 2 M KOH electrolyte. The specific capacity (Q_s) and specific capacitance (C_s) were calculated from the discharge curve using the following formulas [43]:

$$Q_s = \frac{\int i(A) \times dt(s)}{m \times 3600} \quad (A1)$$

$$C_s = \frac{Q_s \times 3600}{\Delta V} \quad (A2)$$

where i , Δt , m , and ΔV are the discharge current density (A), discharge time (s), mass of the active material (g), and potential window (V), respectively.

Appendix A.3. Asymmetric Supercapacitor Device Based on α -Fe₂O₃-NF//Co₃O₄-NF

To fabricate a flexible asymmetric supercapacitor device, α -Fe₂O₃-NF and Co₃O₄-NF electrodes were used as the negative and positive electrodes, respectively. PVA-KOH was used as the gel polymer electrolyte and separator. The PVA-KOH electrolyte was prepared using a previously reported method [44]. The α -Fe₂O₃-NF and Co₃O₄-NF electrodes were painted with the PVA-KOH electrolyte and allowed to solidify at room temperature. This process was repeated 2 to 3 times to ensure that a sufficient amount of electrolyte was coated on the electrode surface. After the solidification process, the two electrodes were sandwiched, and the device was packed and tested. The C_s , energy density, and power density values were calculated using a previously reported formula [42]. The charges

between the cathode and anode can be balanced for excellent electrochemical results for the ASC device using the theory of mass balance as per the following equation:

$$\frac{m_+}{m_-} = \frac{C_- \times \Delta V_-}{C_+ \times \Delta V_+} \quad (\text{A3})$$

where $m_{(+ \text{ or } -)}$, $\Delta V_{(+ \text{ or } -)}$, and $C_{(+ \text{ or } -)}$ are the mass of the active material (g), potential window (ΔV), and C_s (F/g) of the positive and negative electrodes, respectively. The mass ratio calculated between the positive and the negative electrodes is 1:1.56. The specific capacitance (C_{sc} , F/g), specific energy (E , Wh/kg), and specific power (P , W/kg) of the ASC cell were calculated using the following equations:

$$C_{sc} = \frac{I \times \Delta t}{m \times \Delta V} \quad (\text{A4})$$

$$E = \frac{0.5 \times C_{sc} \times \Delta V^2}{3.6} \quad (\text{A5})$$

$$P = \frac{E \times 3600}{\Delta t} \quad (\text{A6})$$

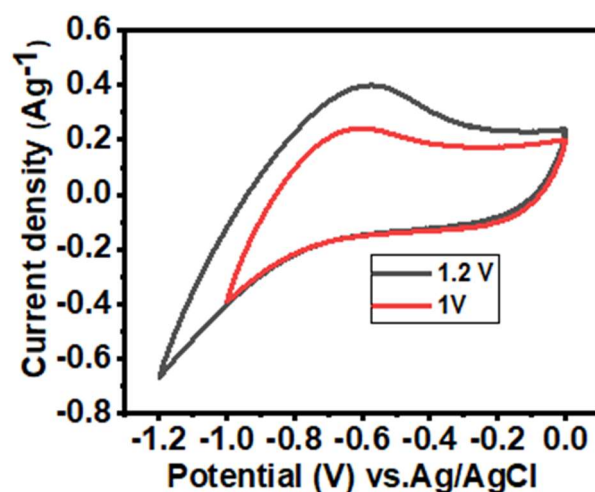


Figure A1. CV curves for $\alpha\text{-Fe}_2\text{O}_3\text{-NF}$ in -1 V and -1.2 V at 100 mV/s.

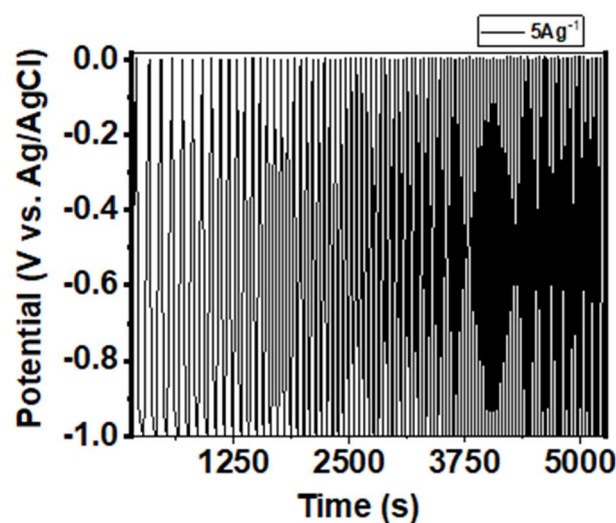


Figure A2. Stability test results for 5000 charge-discharge cycles at a current density of 5 A/g.

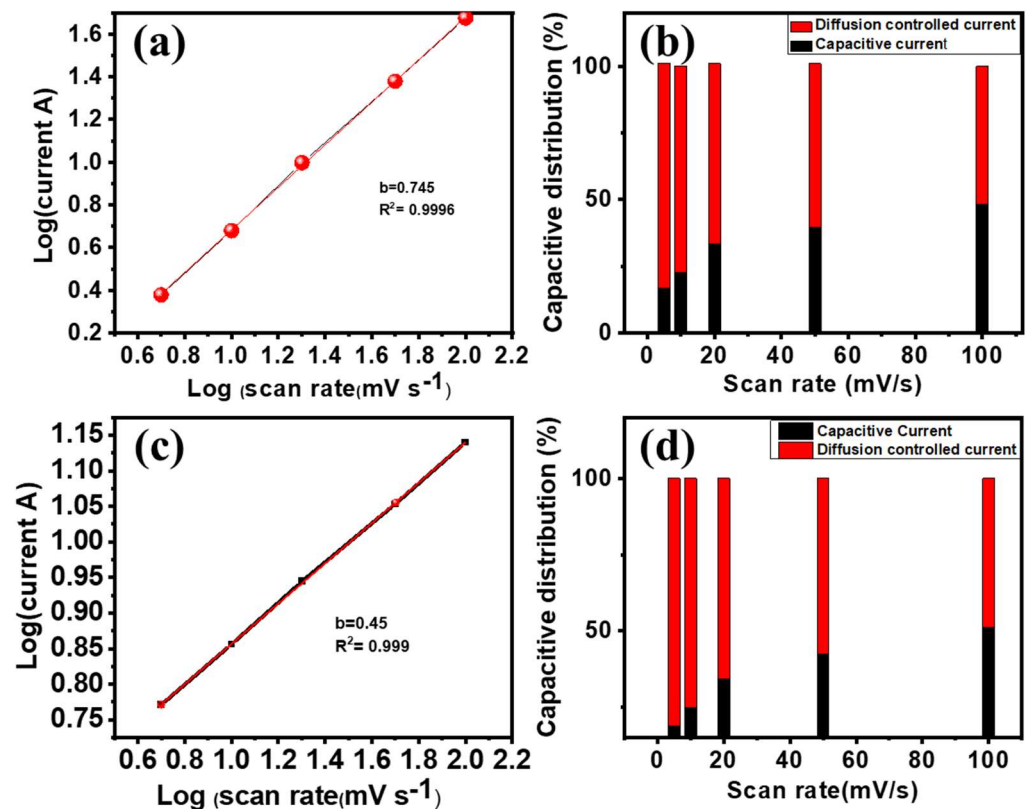


Figure A3. (a,c) Plot of current vs. scan rate in log-scale to calculate the b-value, (b,d) the plot of capacitive and diffusion-controlled current contributions with scan rates corresponding to Fe₂O₃ and Co₃O₄, respectively.

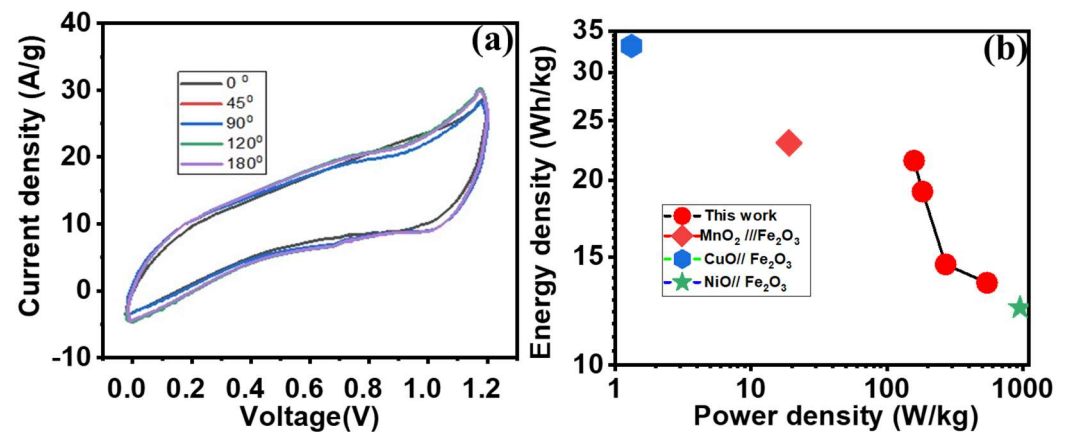


Figure A4. (a) CV curves at different angles, (b) the Ragone plot for the Co₃O₄-NF//Fe₂O₃-NF ASC device.

Table A1. The electrochemical performance of the ferric-oxide-based negative electrode.

Material	Electrolyte	Capacitance	Stability	Ref.
Fe ₂ O ₃ /CF	5 M LiCl	180.4 mF/cm ²	-	[44]
Fe ₂ O ₃ -C	3 M KOH	247.5 mAh/g (2 mV/s)	64% (5000)	[42]
Fe ₂ O ₃ NF	5 M LiCl	145.9 mF/cm ² 10 mA/cm ²	87.2% (5000)	[45]
Fe ₂ O ₃ @C	6 M KOH	304.9 at 1 A/g	90.7% (2000)	[46]
CF-Fe ₂ O ₃	2 M KOH	1.56 F/cm ² at 10 mA/cm ²	102% (5000)	[47]

Table A1. Cont.

Material	Electrolyte	Capacitance	Stability	Ref.
Fe ₂ O ₃ /CF	0.5 M LiClO ₄	261 F/g at 1 A/g	82.7% (10,000)	[48]
Fe ₂ O ₃ /CF	2 M KOH	908 F/g at 10 A/g	90% (5000)	[36]
Fe ₂ O ₃ -NF	2 M KOH	2125 F/g at 4 A/g	95.2% (5000)	Present work

Table A2. The electrochemical performance of the ferric-oxide-based ASC devices.

ASC Devices	Electrolyte	Specific Capacitance	Energy Density	Power Density	Ref.
CuO//Fe ₂ O ₃	CMC-Na ₂ SO ₄	79 F/g	23 Wh/kg	19 kW/kg	[49]
MnO ₂ @CuO//Fe ₂ O ₃ @C	PVA-LiCl	2.46 F/cm ³ (0.13 A/cm ²)	0.85 mWh/cm ³	0.1 W/cm ³	[50]
CF-Co ₃ O ₄ //CF-Fe ₂ O ₃	PVA-KOH	17.5 F/cm ³ (6 mA/cm ²)	6.75 mWh/cm ³	104 mW/cm ³	[51]
MnO ₂ //Fe ₂ O ₃	PVA-LiClO ₄	74 F/g (5 mV/s)	33.1 Wh/kg	1.32 kW/kg	[44]
MnO ₂ //Fe ₂ O ₃	PVA-LiCl	1.21 F/cm ³ (0.5 mA/cm ²)	0.41 mWh/cm ³	-	[51]
MnO ₂ /CF//Fe ₂ O ₃ /CF	PVA-LiCl	1.5 F/cm ³ (0.5 mA/cm ²)	0.55 mWh/cm ³	-	[44]
NiO//Fe ₂ O ₃	PVA KOH	57.2 F/g	12.4 Wh/kg	951 W/kg	[32]
Co ₃ O ₄ -NF//Fe ₂ O ₃ -NF	PVA KOH	155 F/g	21.5 Wh/kg	158 kW/kg	Present work

References

- Miller, J.R.; Simon, P. Electrochemical capacitors for energy management. *Science* **2008**, *321*, 651–652. [\[CrossRef\]](#) [\[PubMed\]](#)
- Simon, P.; Gogotsi, Y. Materials for electrochemical capacitors. *Nat. Mat.* **2008**, *7*, 845–854. [\[CrossRef\]](#) [\[PubMed\]](#)
- Zhou, Q.; Xing, J.; Gao, Y.; Lv, X.; He, Y.; Guo, Z.; Li, Y. Ordered assembly of NiCo₂O₄ multiple hierarchical structures for high-performance pseudocapacitors. *ACS Appl. Mater. Interfaces* **2014**, *6*, 11394–11402. [\[CrossRef\]](#) [\[PubMed\]](#)
- Du, J.; Zhou, G.; Zhang, H.; Cheng, C.; Ma, J.; Wei, W.; Chen, L.; Wang, T. Ultrathin porous NiCo₂O₄ nanosheet arrays on flexible carbon fabric for high-performance supercapacitors. *ACS Appl. Mater. Interfaces* **2013**, *5*, 7405–7409. [\[CrossRef\]](#)
- Zhou, W.; Kong, D.; Jia, X.; Ding, C.; Cheng, C.; Wen, G. NiCo₂O₄ nanosheet supported hierarchical core-shell arrays for high-performance supercapacitors. *J. Mater. Chem. A* **2014**, *2*, 6310–6315. [\[CrossRef\]](#)
- Cai, D.; Xiao, S.; Wang, D.; Liu, B.; Wang, L.; Liu, Y.; Li, H.; Wang, Y.; Li, Q.; Wang, T. Morphology controlled synthesis of NiCo₂O₄ nanosheet array nanostructures on nickel foam and their application for pseudocapacitors. *Electrochim. Acta* **2014**, *142*, 118–124. [\[CrossRef\]](#)
- Zhang, G.; Lou, X. Controlled growth of NiCo₂O₄ nanorods and ultrathin nanosheets on carbon nanofibers for high-performance supercapacitors. *Sci. Rep.* **2013**, *3*, 1470. [\[CrossRef\]](#)
- Zhou, J.; Huang, Y.; Cao, X.; Ouyang, B.; Sun, W.; Tan, C.; Zhang, Y.; Ma, Q.; Liang, S.; Yan, Q.; et al. Two-dimensional NiCo₂O₄ nanosheet-coated three-dimensional graphene networks for high-rate, long-cycle-life supercapacitors. *Nanoscale* **2015**, *7*, 7035–7039. [\[CrossRef\]](#)
- Li, Y.; Li, Q.; Cao, L.; Cui, X.; Yang, Y.; Xiao, P.; Zhang, Y. The impact of morphologies and electrolyte solutions on the supercapacitive behavior for Fe₂O₃ and the charge storage mechanism. *Electrochim. Acta* **2015**, *178*, 171–178. [\[CrossRef\]](#)
- Zhang, G.; Lou, X.W. General solution growth of mesoporous NiCo₂O₄ nanosheets on various conductive substrates as high-performance electrodes for supercapacitors. *Adv. Mater.* **2013**, *25*, 976–979. [\[CrossRef\]](#)
- Nithya, V.D.; Arul, N.S. Progress and development of Fe₃O₄ electrodes for supercapacitors. *J. Mater. Chem. A* **2016**, *4*, 10767–10778. [\[CrossRef\]](#)
- Khatavkar, S.N.; Sartale, S.D. α -Fe₂O₃ thin films by liquid phase deposition: Low-cost option for supercapacitor. *J. Solid State Electrochem.* **2016**, *21*, 2555–2566. [\[CrossRef\]](#)
- He, Y.M.; Chen, W.J.; Li, X.D.; Zhang, Z.X.; Fu, J.C.; Zhao, C.H.; Xie, E.Q. Freestanding three-dimensional graphene/MnO₂ composite networks as ultralight and flexible supercapacitor electrodes. *ACS Nano* **2013**, *7*, 174–182. [\[CrossRef\]](#) [\[PubMed\]](#)
- Meng, W.; Wei, C.; Lei, Z.; Yang, H.; Zhu, M.; Yan, H.; Fu, Y.; Geng, F.; Jie, Y.; Chen, X. Porous Fe₃O₄/carbon composite electrode material prepared from metal-organic framework template and effect of temperature on its capacitance. *Nano Energy* **2014**, *8*, 133–140. [\[CrossRef\]](#)
- Li, Y.; Shen, W. Morphology-dependent nanocatalysts: Rod-shaped oxides. *Chem Soc. Rev.* **2014**, *43*, 1543–1574. [\[CrossRef\]](#)
- Mishra, M.; Chun, D.M. Alpha-Fe₂O₃ as a photocatalytic material: A review. *Applied Catalysis A: General. Appl. Catal. A* **2015**, *498*, 126–141. [\[CrossRef\]](#)
- Upadhyay, K.K.; Nguyen, T.; Silva, T.M.; Carmezim, M.J.; Montemor, M.F. Electrodeposited MoOx films as negative electrode materials for redox supercapacitors. *Electrochim. Acta* **2017**, *225*, 19–28. [\[CrossRef\]](#)
- Lu, X.; Yu, M.; Zhai, T.; Wang, G.; Xie, S.; Liu, T.; Liang, C.; Tong, Y.; Li, Y. High energy density asymmetric quasi-solid-state supercapacitor based on porous vanadium nitride nanowire anode. *Nano Lett.* **2013**, *13*, 2628–2633. [\[CrossRef\]](#)

19. Li, J.; Wu, Q.; Zan, G. A high-performance supercapacitor with well-dispersed Bi₂O₃ nanospheres and active-carbon electrodes. *Eur. Inorg. Chem.* **2015**, *201*, 5751–5756. [[CrossRef](#)]
20. Bak, C.; Kim, K.; Jung, K.; Kim, J.B.; Jang, J.H. Efficient photoelectrochemical water splitting of nanostructured hematite on a three-dimensional nanoporous metal electrode. *J. Mater. Chem. A* **2014**, *2*, 17249–17252. [[CrossRef](#)]
21. Nithya, V.D.; Arul, N.S. Review on α -Fe₂O₃ based negative electrode for high performance supercapacitors. *J. Power Sources* **2016**, *327*, 297–318. [[CrossRef](#)]
22. Hunge, Y.M. Photoelectrocatalytic degradation of 4-chlorophenol using nanostructured α -Fe₂O₃ thin films under sunlight illumination. *J. Mar. Sci.* **2017**, *28*, 11260–11267. [[CrossRef](#)]
23. Yadav, A.A.; Hunge, Y.M.; Kulkarni, S.B. Chemical synthesis of Co₃O₄ nanowires for symmetric supercapacitor device. *J. Mar. Sci.* **2018**, *29*, 16401–16409. [[CrossRef](#)]
24. Hjjiri, M. Highly sensitive NO₂ gas sensor based on hematite nanoparticles synthesized by sol–gel technique. *J. Mar. Sci. Eng.* **2020**, *31*, 5025–5031. [[CrossRef](#)]
25. Xiao, T.; Che, P.; Xiao, R.; Xiang, P.; Jiang, L.; Tao, F.; Tan, X.; Chen, X. 3D interconnected Fe-Co-S nanosheets network directly grown on graphene coated nickel foam with enhanced electrochemical performance for asymmetric supercapacitors. *Appl. Surf. Sci.* **2021**, *543*, 148747. [[CrossRef](#)]
26. Zachariasen, W.H. *Skrifterutgittav det Norske Videnskaps-Akademi I Oslo 1: Matematisk—NaturvidenskpelingsKlasse*; New York Botanical Garden: Bronx, NY, USA, 1998; pp. 1–165.
27. Wang, J.-C.; Ren, J.; Yao, H.-C.; Zhang, L.; Wang, J.-S.; Zang, S.-Q.; Han, L.-F.; Li, Z.-J. Synergistic photocatalysis of Cr (VI) reduction and 4-chlorophenol degradation over hydroxylated α -Fe₂O₃ under visible light irradiation. *J. Hazard. Mater.* **2016**, *311*, 11–19. [[CrossRef](#)]
28. McIntyre, N.S.; Zetaruk, D.G. X-ray photoelectron spectroscopic studies of iron oxides. *Anal. Chem.* **1977**, *49*, 1521–1529. [[CrossRef](#)]
29. Grosvenor, A.P.; Kobe, B.A.; Biesinger, M.C.; McIntyre, N.S. Investigation of multiplet splitting of Fe 2p XPS spectra and bonding in iron compounds. *Surf. Interface Anal.* **2004**, *36*, 1564–1574. [[CrossRef](#)]
30. Lee, K.K.; Deng, S.; Fan, H.M.; Mhaisalkar, S.; Tan, H.R.; Tok, E.S.; Loh, K.P.; Chin, W.S.; Sow, C.H. α -Fe₂O₃ nanotubes-reduced graphene oxide composites as synergistic electrochemical capacitor materials. *Nanoscale* **2012**, *4*, 2958–2961. [[CrossRef](#)]
31. Zhang, H.; Gao, Q.; Yang, K.; Tan, Y.; Tain, W.; Zhu, L.; Li, Z.; Yang, C. Solvothermally induced α -Fe₂O₃/graphene nanocomposites with ultrahigh capacitance and excellent rate capability for supercapacitors. *J. Mater. Chem. A* **2015**, *3*, 22005–22011. [[CrossRef](#)]
32. Zhang, S.; Yin, B.; Wang, Z.; Peter, F. Super long-life all solid-state asymmetric supercapacitor based on NiO nanosheets and α -Fe₂O₃ nanorods. *Chem. Eng. J.* **2016**, *306*, 193–203. [[CrossRef](#)]
33. Chen, Y.; Kang, C.; Ma, L.; Fu, L.; Li, G.; Hu, Q.; Liu, Q. MOF-derived Fe₂O₃ decorated with MnO₂ nanosheet arrays as anode for high energy density hybrid supercapacitor. *Chem. Eng. J.* **2021**, *417*, 129243. [[CrossRef](#)]
34. Tang, D.; Wang, W.; Wang, G. The perfect matching between the low-cost Fe₂O₃ nanowire anode and the NiO nanoflake cathode significantly enhance the energy density of asymmetric supercapacitors. *J. Mater. Chem. A* **2015**, *3*, 6662–6670. [[CrossRef](#)]
35. Yadav, A.A.; Hunge, Y.M.; Liu, S.; Kulkarni, S.B. Ultrasound assisted growth of NiCo₂O₄@carbon cloth for high energy storage device application. *Ultrason. Sonochem.* **2019**, *56*, 290–292. [[CrossRef](#)]
36. Yuan, C.; Yang, L.; Hou, L.; Shen, L.; Zhang, X.; Lou, X.W. Growth of ultrathin mesoporous Co₃O₄ nanosheet arrays on Ni foam for high-performance electrochemical capacitors. *Energy Environ. Sci.* **2012**, *5*, 7883–7887. [[CrossRef](#)]
37. Zheng, Y.; Li, Z.; Xu, J.; Wang, T.; Liu, X.; Duan, X.; Ma, Y.; Zhou, Y.; Pei, C. Multi-channeled hierarchical porous carbon incorporated Co₃O₄ nanopillar arrays as 3D binder-free electrode for high performance supercapacitors. *Nano Energy* **2016**, *20*, 94–107. [[CrossRef](#)]
38. Demarconnay, L.; Raymundo-Pinero, E.; Beguin, F. Adjustment of electrodes potential window in an asymmetric carbon/MnO₂ supercapacitor. *J. Power Sources* **2011**, *196*, 580–586. [[CrossRef](#)]
39. Sahoo, R.; Roy, A.; Ray, C.; Mondal, C.; Negishi, Y.; Yusuf, S.M.; Pal, A.; Pal, T. Decoration of Fe₃O₄ base material with Pd loaded CdS nanoparticle for superior photocatalytic efficiency. *J. Phys. Chem. C* **2014**, *118*, 11485–11494. [[CrossRef](#)]
40. Chen, J.; Wang, Y.; Cao, J.; Liu, Y.; Ouyanga, J.; Jia, D.; Zhou, Y. Flexible and solid-state asymmetric supercapacitor based on ternary graphene/MnO₂/carbon black hybrid film with high power performance. *Electrochim. Acta.* **2015**, *182*, 861–870. [[CrossRef](#)]
41. Yadav, A.A.; Hunge, Y.M.; Kulkarni, S.B. Synthesis of multifunctional FeCo₂O₄ electrode using ultrasonic treatment for photocatalysis and energy storage. *Ultrason. Sonochem.* **2019**, *58*, 104663. [[CrossRef](#)]
42. Li, R.; Wang, Y.; Zhou, C.; Wang, C.; Ba, X.; Li, Y.; Huang, X.; Liu, J. Carbon-stabilized high-capacity ferroferric oxide nanorod array for flexible solid-state alkaline battery–supercapacitor hybrid device with high environmental suitability. *Adv. Funct. Mater.* **2015**, *25*, 5384–5394. [[CrossRef](#)]
43. Chodankar, N.R.; Pham, H.D.; Nanjundan, A.-K.; Fernando, J.F.S.; Jayaramulu, K.; Golberg, D.; Han, Y.-K.; Dubal, D.P. True meaning of pseudocapacitors and their performance metrics: Asymmetric versus hybrid supercapacitors. *Small* **2020**, *16*, 2002806. [[CrossRef](#)] [[PubMed](#)]
44. Yang, P.; Ding, Y.; Lin, Z.; Chen, Z.; Li, Y.; Qiang, P.; Ebrahimi, M.; Mai, W.; Wong, C.P.; Wang, Z.L. Low-Cost High-Performance Solid-State Asymmetric Supercapacitors Based on MnO₂ Nanowires and Fe₂O₃ Nanotubes. *Nano Lett.* **2014**, *14*, 731–736. [[CrossRef](#)] [[PubMed](#)]

45. Wang, H.; Xu, Z.; Yi, H.; Wei, H.; Guo, Z.; Wang, X. One-step preparation of single-crystalline Fe₂O₃ particles/graphene composite hydrogels as high-performance anode materials for supercapacitors. *Nano Energy* **2014**, *7*, 86–96. [[CrossRef](#)]
46. Yan, Y.; Tang, H.; Wu, F.; Wang, R.; Pan, M. One-step self-assembly synthesis α -Fe₂O₃ with carbon-coated nanoparticles for stabilized and enhanced supercapacitors electrode. *Energies* **2017**, *10*, 1296. [[CrossRef](#)]
47. Li, T.; Yu, H.; Zhi, L.; Zhang, W.; Dang, L.; Liu, Z.; Lei, Z. Facile electrochemical fabrication of porous Fe₂O₃ nanosheets for flexible asymmetric supercapacitors. *J. Phys. Chem. C* **2017**, *121*, 18982–18991. [[CrossRef](#)]
48. Cho, S.; Patil, B.; Yu, S.; Ahn, S.; Hwang, J.; Park, C.; Do, K.; Ahn, H. Flexible swiss roll fiber-shaped asymmetric supercapacitor using MnO₂ and Fe₂O₃ on carbon fibers. *Electrochim. Acta* **2018**, *269*, 499–508. [[CrossRef](#)]
49. Shinde, A.V.; Chodankar, N.R.; Lokhande, A.C.; Ji, T.; Kim, J.H.; Lokhande, C.D. Highly energetic flexible all-solid-state asymmetric supercapacitor with Fe₂O₃ and CuO thin films. *RSC Adv.* **2016**, *6*, 58839–58843. [[CrossRef](#)]
50. Yu, Z.; Moore, J.; Calderon, J.; Zhai, L.; Thomas, J. Coil-Type Asymmetric Supercapacitor/Electrical Cables. *Small* **2015**, *11*, 5289–5295. [[CrossRef](#)]
51. Lu, X.; Zeng, Y.; Yu, M.; Zhai, T.; Liang, C.; Xie, S.; Balogun, M.S.; Tong, Y. Oxygen-deficient hematite nanorods as high-performance and novel negative electrodes for flexible asymmetric supercapacitors. *Adv. Mater.* **2014**, *26*, 3148–3155. [[CrossRef](#)]